Published in final edited form as:

Biomed Tech (Berl). 2015 October ; 60(5): 457–463. doi:10.1515/bmt-2015-0048.

Extended arrays for nonlinear susceptibility magnitude imaging

Bradley W. Ficko, **Paolo Giacometti**, and **Solomon G. Diamond**[*]

Thayer School of Engineering at Dartmouth, Hanover, NH 03755, USA

Abstract

This study implements nonlinear susceptibility magnitude imaging (SMI) with multifrequency intermodulation and phase encoding. An imaging grid was constructed of cylindrical wells of 3.5-mm diameter and 4.2-mm height on a hexagonal two-dimensional 61-voxel pattern with 5-mm spacing. Patterns of sample wells were filled with 40-μl volumes of Fe_3O_4 starch-coated magnetic nanoparticles (mNPs) with a hydrodynamic diameter of 100 nm and a concentration of 25 mg/ml. The imaging hardware was configured with three excitation coils and three detection coils in anticipation that a larger imaging system will have arrays of excitation and detection coils. Hexagonal and bar patterns of mNP were successfully imaged ($R^2 > 0.9$) at several orientations. This SMI demonstration extends our prior work to feature a larger coil array, enlarged field-of-view, effective phase encoding scheme, reduced mNP sample size, and more complex imaging patterns to test the feasibility of extending the method beyond the pilot scale. The results presented in this study show that nonlinear SMI holds promise for further development into a practical imaging system for medical applications.

Keywords

magnetic nanoparticles; magnetic susceptibility; nonlinear; tomographic imaging

Introduction

Magnetic nanoparticles (mNP) hold great promise for use in medicine in conjunction with targeted therapeutics and as imaging contrast agents. Over the past decade, researchers have begun to understand how to exploit the unique magnetic properties of mNPs for medical imaging applications [21, 22]. The three primary methods that have emerged are magnetic susceptibility imaging [3–5, 14, 20, 30], magnetic relaxometry (MRX) [1, 6, 15, 17, 18, 24–26, 28, 31], and magnetic nanoparticle imaging (MPI) [2, 10–12, 16, 23, 29, 27]. Our group has recently introduced several new algorithms for mNP imaging in methods we call susceptibility magnitude imaging (SMI) [9], spectroscopic AC susceptibility imaging (sASI) [8], and nonlinear susceptibility magnitude imaging (nSMI) [7]. In these three methods for mNP imaging, we emphasize the use of lower-cost hardware with advanced computational methods rather than higher-end hardware solutions. The focus of the present study is to demonstrate that nonlinear SMI is a scalable approach to mNP imaging by developing it significantly beyond the concept-level demonstration of our prior work. The long-term

[*]Corresponding author: Solomon G. Diamond, Thayer School of Engineering at Dartmouth, 14 Engineering Drive, Hanover, NH 03755, USA, Phone: +1-603-646-1311, Fax: +1-603-646-3856, Solomon.G.Diamond@Dartmouth.edu.

development objective of nonlinear SMI is to deliver an affordable and portable, high-resolution mNP imager for clinical point-of-care diagnostics (Figure 1A).

In nonlinear SMI, an AC magnetic field having a gradient across the imaging zone causes partial magnetic saturation of mNPs that are used as a contrast agent. Owing to the gradient of the applied magnetic field, the degree of saturation of the mNPs will vary with spatial location. Detection coils can measure harmonics that arise due to the saturation nonlinearity. Tuning the detection coils to these frequencies and applying tomographic imaging methods enable images to be generated from the data. Harmonics from nonlinear saturation effects can be created with a single frequency or from the interaction of multiple frequencies, which produces signals at intermodulation frequencies.

To capture enough imaging data to produce high-resolution tomographic images, a phase encoding scheme may be used to obtain spatial information above and beyond what can be obtained from the harmonic and intermodulation frequencies alone. A conceptual illustration of a phase encoding scheme is shown in Figure 1. In Figure 1B, the coils are labeled, and an example sensitivity map is shown. This sensitivity map represents an average signal measured by the detection coils for a unit quantity of mNP sample located in each of the 61 voxels. In this illustration, all three excitation coils are driven at the same frequency, which makes it possible to shift the phase of the coils relative to each other and cause a shift in the magnetic field gradients throughout the imaging area. The spatial sensitivity effects of implementing phase rotations and how this further varies with harmonics is shown in Figure 1C.

Our prior work in nonlinear SMI was at a pilot scale with minimal imaging complexity and only 12 imaging voxels. In the present study, we have extended our imaging capabilities to 61 voxels in a 4.5-cm hexagonal imaging grid. This report details several steps toward implementation of a larger-scale imaging array. We have extended our hardware to three excitation coils and three detection coils. We have successfully implemented a phase-encoding scheme using two frequencies and demonstrated that it is possible to reconstruct higher-density images. We also enlarged the field-of-view while simultaneously reducing the mNP sample size and demonstrate the system with more complex imaging patterns. The results presented here demonstrate the feasibility of extending the method beyond the pilot scale and allow us to continue on the development path toward a high-resolution imaging system that is suitable for medical imaging applications.

Materials and methods

Analog and digital systems

The experimental setup had six coils as depicted in (Figure 2). The coils (Jantzen-1257, 0.3 mm diameter wire, 7 mH, 11.8 Ω at DC, 15 mm inner diameter × 15 mm height × 26 mm outer diameter, Jantzen, Praestoe, Denmark) were arranged under and around a hexagonal imaging grid. The excitation coils were positioned 1 mm under the imaging grid in a triangular configuration to provide an AC magnetic gradient field across the imaging zone. The three coils arranged around the outside of the imaging grid for use as detection coils and were positioned 1 mm from the edge of the imaging region. A removable, laser-cut hexagonal grid with 5-mm spacing was used to place mNP samples in 61 cylindrical wells. The cylindrical wells were 3.5 mm diameter and 4.2 mm in height. A hexagonal imaging grid was chosen because of its symmetry relative to the excitation and detection coils. The hexagonal symmetry of the grid also expedited the calibration of the imaging matrix because each calibration sample template could be repositioned six times as described in the "Experimental setup" section. The design of the electronics hardware was previously described [7, 9]. This prior work also describes the link between analog and digital processes and the workflow for generating AC currents, measurement, and postprocessing of acquired magnetization responses. To achieve higher currents than in previous studies, a resonant circuit was constructed for each of the excitation coils using capacitors of 20 μF and tuned to two frequencies (327 and 350 Hz). The electric current in each of the excitation coils was approximately 600 mA peak-to-peak and produced magnetic fields of approximately 10 mT in the center of the excitation coils. A DC magnetic field gradient was also created by positioning three vertical stacks of four neodymium permanent magnets located 3.5 cm from the imaging zone and one neodymium magnet positioned in plane with each detection coil.

Nanoparticles

Testing was performed using Fe_3O_4 starch-coated mNPs with a hydrodynamic diameter of 100 nm (10-00-102, micromod Partikeltechnologie GmbH, Rostock, Germany). All samples were at a concentration of 25 mg/ml. A volume of 40 μl of mNP solution was pipetted into the cylindrical wells at desired locations. Lids of 1.5-mm-thick acrylic were epoxied onto the imaging grids to provide a waterproof seal. Fourteen imaging grids were created, and MNP samples were pipetted into 11 locations for calibration and several spatial patterns for imaging. The magnetic properties of these mNPs have been previously characterized by [13, 19].

Imaging and data processing

The experimental phase encoding scheme is shown in Table 1. The experimental system uses two frequencies on each coil (327 and 350 Hz) such that both harmonic and intermodulation frequencies can be used for image reconstruction.

The phase encoding used four phase rotations with different phases for each frequency. The two frequencies have an initial $\pi/2$ phase shift such that the magnetic field spatial patterns are well separated and do not mirror one another. The applied magnetic fields used in our experimental configuration are capable of producing a susceptibility response from the mNPs that contains the second and third harmonics, as well as the second and third intermodulation frequencies (Table 2). When measured with three detection coils, this produces 27 data channels per phase setting, and so by using four phase rotations, we can capture 108 data channels. By splitting the measurements into in-phase and out-of-phase measurements, the number of data channels doubles to 216. These 216 data channels are then used to create 61-voxel nonlinear SMIs. The data processing and imaging workflow for this process have been previously detailed [7] and not reproduced here. The same non-negative least squares inversion of the imaging matrix was used in the present study. However, in our previous report, the imaging matrix consisted of only 12 voxels, whereas the present study uses 61 voxels. The computational methods for image reconstruction are otherwise identical.

Experimental setup

To demonstrate high density nonlinear SMI, we conducted a study using a 61-voxel imaging grid. Initially, a calibration was performed by splitting the imaging grid into 10 regions of grid locations (minus the center point) that each comprise one sixth of the imaging grid. A calibration sample template was created for each of these 10 grid regions containing an mNP sample. The calibration data was obtained by measuring the response to the calibration sample at each of the four phase rotations before reorienting the calibration sample through the remaining five orientations that make up a full set of placements around the hexagonal imaging grid. Data was acquired at each phase rotation for 8 s before shifting to the next phase. An initial 8-s buffer was used to allow time to place the calibration sample. Therefore, the measurement time for obtaining calibration data at each location on the imaging grid was 40 s. To help reduce drift and systematic error from the mechanical motion of the apparatus when a sample was placed and withdrawn, a baseline measurement without the calibration sample present was obtained before acquiring the six positions with the sample present. Interleaving these baseline measurements was expected to help improve the accuracy of the calibration data. The baseline measurements also took 40 s, making the total measurement time 80 s per grid location.

Once all 61 calibration points were measured, a calibration matrix was constructed according to our previous report on nonlinear SMI [7] but extended to 61-voxel locations. With the calibration matrix fully constructed, nonlinear SMIs were obtained from mNP samples arranged into hexagonal and bar patterns. In addition, a hexagonal saline pattern was also imaged to ensure that imaging contrast was specific to the mNP samples and not saline or other materials in the mNP sample holder. Each measurement of these sample patterns required 40 s to capture and was accompanied with a 40-s baseline measurement. The images were then reconstructed using a non-negative least squares function (lsqnonneg) in Matlab (The MathWorks Inc., Natick, MA, USA).

Results

Owing to the potential for variability from manual placement of mNP samples, three calibration data sets were obtained. This variability was quantified by visualizing a point spread function matrix that was obtained by multiplying one calibration data set by the inverse of another (Figure 3). This test assesses the consistency of the calibration procedure when placing the samples in each of the 61 locations and then repositioning them later in the same positions several hours later. The ideal result would be an identity matrix of dimensions 61 × 61. The point spread function matrix that we obtained matched to an identity matrix with $R^2 = 0.92$.

The calibration matrix was optimized by choosing the median of each matrix element from the three calibration sets and then keeping the best 138 data rows in the calibration matrix when ranked in order of increasing deviations from the median. This truncation level was chosen by optimizing the point spread function analysis shown in Figure 3. Tomographic images were produced with patterns positioned in the imaging field of view. The first two shapes, a hexagon and a bar pattern, contained mNPs, while a third hexagon pattern with saline contained no mNPs. SMIs obtained compared to the ground truth expected images are shown. In the case of the hexagon and the bar patterns, the sample was rotated through the imaging grid six times to produce an image of each pattern at six orientations. The saline sample was placed in three different orientations.

In Figure 4, three hexagonal patterns are shown in various orientations on the imaging grid. These three had the highest R^2 values of the set of six at 0.94, 0.90, and 0.92, respectively. The remaining three hexagonal pattern SMIs are not shown, but the R^2 values were 0.85, 0.80, and 0.78.

In Figure 5, three bar patterns are shown in various orientations in the imaging grid. These three bar patterns that had the best R^2 values at 0.96, 0.96, and 0.97, respectively. The remaining three SMIs of the bar patterns are not shown but had R^2 values of 0.95, 0.94, and 0.66.

In Figure 6, a single SMI of a hexagon pattern of saline is shown. The image has an R^2 value of 0.01. The other saline images were similar and are not shown.

Discussion

In this study, we built upon our prior work in nonlinear SMI and extended its imaging capabilities to 61 voxels on a hexagonal imaging grid of 4.5 cm in diameter. We successfully implemented a phase-encoding scheme that modulated the phase of two frequencies across three excitation coils. Using the spatial information contained in harmonic frequencies and the different spatial patterns created with phase modulation, it was possible to reconstruct mNP images of hexagonal and bar patterns. In addition, we showed that a hexagonal pattern of saline was not recoverable, meaning that the SMI contrast was selective to the mNP samples.

To extend the imaging capabilities, we increased the number of excitation and detection coils to three and reduced the mNP sample volume from 500 μl in our prior work to 40 μl in the present study. Overall, we improved our system and successfully increased the number of voxels by a factor of 5, reduced the sample size by a factor of more than 10, more than doubled the field-of-view of the imaging zone, and successfully imaged more complex mNP patterns. Together, these advancements represent a critical milestone toward scaling up nonlinear SMI to a size and imaging density that has utility in medical imaging applications.

We produced images of hexagonal and bar patterns, and the quality of the images varied noticeably. In the best cases, the images were quite good with R^2-values as high as 0.97, while the poorest image reconstruction had an R^2 of 0.66. We noticed that the positions that worked best and worst were not necessarily consistent between tests or across the two patterns that were tested. This led us to believe that much of the error in image reconstruction may have been due to the inaccuracy of manually placing the samples and the quality of the sample holder. The sample holders were laser cut from acrylic, leading to some warping and inconsistency in the size of the cylindrical wells. In addition, the top and bottom lids were manually epoxied into place leading to some misalignment and uneven surface finish around the perimeter. In future studies, we plan to mill the sample holder leading to much more consistent sample wells. In addition, we are working on building an analytic forward model to help reduce the amount of manual calibration necessary for imaging. These improvements should help reduce the inconsistencies in the imaging calibration process and lead to improved and more consistent imaging results.

In this study, the images had 5-mm voxel spacing. However, the sample size was only 40 μl, which could fit into voxels of dimensions of 3.5 mm × 3.5 mm × 4.2 mm. The larger grid spacing used in the present study helped to distinguish adjacent voxels, but we believe that given the high signal levels that we receive from each of the 61 locations, it will be possible to shrink the dimensions of the voxels in the future. In order to accurately image with higher spatial density, it will be necessary to improve the quality of the samples and to use additional phase rotations for encoding. Both of these improvements are feasible and should help boost the number of voxels in an image to exceed 100 and reduce the voxel spacing to < 5 mm.

In future work, we would like to demonstrate three-dimensional images. In the present configuration, the mNPs were located close to the excitation coils, and therefore, high sensitivity was achieved. As the mNPs move away from the excitation coils, sensitivity will diminish and imaging will become more difficult. We believe that with the present configuration, we can create images up to one radius distance (~1 cm) away from the excitation coils. To achieve depth resolution beyond that range, it may be necessary to use larger coils and additional encoding schemes.

We found in this study that SMI is selectively sensitive to mNPs over saline, and after some further improvements to the spatial resolution, it will be appropriate to shift to *in vivo* experimentation. To realize SMI as a useful medical imaging technology, we believe that it will ultimately be necessary to scale up the system until 1-mm resolution is achieved. In the present work, we added additional excitation and detection coils, and we believe that further expansion is possible. In order to reduce the imaging resolution to the 1-mm scale, it will be necessary to increase the magnetic field strength beyond the few millitesla level used in the present study and to use excitation coils that are capable of delivering tens of milliteslas at several centimeters of depth. This increase in field strength will add some additional size and complexity to our current system but could ultimately prove invaluable for high-density imaging as the higher magnetic field gradients will provide many more harmonics and intermodulation frequencies.

The imaging resolution of nonlinear SMI is related to the number of excitation and detection coils, harmonic and intermodulation frequencies detected, and phase-encoding positions. The maximum number of voxels that can be imaged is the product of the number of unique frequencies per excitation coil, detection coils, detected harmonic and intermodulation frequencies, and phase-encoding positions. In our case, we had the same frequencies on all excitation coils, three detection coils, and four phase-encoding positions for a maximum of 108-voxel reconstruction. Owing to some amount of colinearity in the phase-encoding positions and not all harmonics frequencies being above the noise floor in all phase rotations, we were able to reconstruct 61 voxels out of the maximum of 108 even with considerable error from placement of the imaging samples. We believe that as we scale up the design of the imager by adding more excitation and detection coils and by using more phase rotations, it will become possible to achieve a much higher imaging resolution.

Planned future work also includes the development of an analytical imaging model that captures the nonlinear material properties of the mNPs and the field interactions from the arrangement of excitation and detection coils. In the present work, image reconstruction is limited to the voxels that were included in the empirical calibration matrix. This means that image reconstructions can be created with mNP distributions that vary in concentration, but mNPs must remain on the original calibration grid. In addition, images cannot be created at higher or lower resolution except by interpolation in postprocessing. This is because the nonlinearity in the imaging model even between adjacent voxels is potentially high. Interpolation between calibration points could, thus, lead to inaccurate image reconstructions. An analytical imaging model will overcome these limitations.

The present study has demonstrated that nonlinear SMI is a scalable method that can be further developed toward medical imaging applications. We plan to continue working to increase the voxel density while increasing resolution and ultimately translate SMI to *in vivo* imaging.

Acknowledgments

This work was supported, in part, by the National Institutes of Health grants 1R21EB016241-01A1, U54-CA151662, and 5-R24-HD065703. The authors gratefully acknowledge the assistance of Josh Page and Kelly Leonard.

References

1. Adolphi NL, Butler KS, Lovato DM, et al. Imaging of Her2-targeted magnetic nanoparticles for breast cancer detection: comparison of SQUID-detected magnetic relaxometry and MRI. Contrast Media Mol Imaging. 2012; 7:308–319. [PubMed: 22539401]
2. Borgert, J.; Gleich, B.; Buzug, TM. Handbook of medical technology. Berlin, Heidelberg: Springer; 2011. Magnetic particle imaging; p. 461-476.
3. Chieh JJ, Hong CY. Non-invasive and high-sensitivity scanning detection of magnetic nanoparticles in animals using high-T-c scanning superconducting-quantum-interference-device biosusceptometry. Rev Sci Instrum. 2011; 82:84301.
4. Dieckhoff JH, Yoshida T, Enpuku K, Schilling M, Ludwig F. Homogeneous bioassays based on the manipulation of magnetic nanoparticles by rotating and alternating magnetic fields – a comparison. IEEE Trans Magnetics. 2012; 48:3792–3795.
5. Enpuku K, Tamai Y, Mitake T, Yoshida T, Matsuo M. AC susceptibility measurement of magnetic markers in suspension for liquid phase immunoassay. J Appl Phys. 2010; 108:34701.
6. Enpuku K, Watanabe H, Higuchi Y, et al. Characterization of magnetic markers for liquid-phase immunoassays using Brownian relaxation. Jpn J Appl Phys. 2012; 51:23002.
7. Ficko BW, Giacometti P, Diamond SG. Nonlinear susceptibility magnitude imaging of magnetic nanoparticles. J Magn Magn Mater. 2015; 378:267–277. [PubMed: 25505816]
8. Ficko BW, Nadar PM, Diamond SG. Spectroscopic AC susceptibility imaging (sASI) of magnetic nanoparticles. J Magn Magn Mater. 2015; 375:164–176. [PubMed: 25477704]
9. Ficko BW, Nadar PM, Hoopes PJ, Diamond SG. Development of a magnetic nanoparticle susceptibility magnitude imaging array. Phys Med Biol. 2014; 59:1047–1071. [PubMed: 24504184]

10. Gleich B, Weizenecker R. Tomographic imaging using the nonlinear response of magnetic particles. Nature. 2005; 435:1214–1217. [PubMed: 15988521]
11. Goodwill PW, Saritas EU, Croft LR, et al. X-Space MPI: magnetic nanoparticles for safe medical imaging. Adv Mater. 2012; 24:3870–3877. [PubMed: 22988557]
12. Goodwill PW, Scott GC, Stang PP, Conolly SM. Narrowband magnetic particle imaging. IEEE Trans Med Imaging. 2009; 28:1231–1237. [PubMed: 19211340]
13. Gruttner C, Müller K, Teller J, Westphal F, Foreman A, Ivkov R. Synthesis and antibody conjugation of magnetic nanoparticles with improved specific power absorption rates for alternating magnetic field cancer therapy. J Magn Magn Mater. 2007; 311:181–186.
14. Herrera AP, Barrera C, Zayas Y, Rinaldi C. Monitoring colloidal stability of polymer-coated magnetic nanoparticles using AC susceptibility measurements. J Colloid Interface Sci. 2010; 342:540–549. [PubMed: 19948339]
15. Janosek M, Ripka P, Platil A. Magnetic markers detection using PCB fluxgate array. J Appl Phys. 2009; 105:7, E717.
16. Knopp, T.; Buzug, TM. Magnetic particle imaging: an introduction to imaging principles and scanner instrumentation. Berlin, Heidelberg: Springer; 2012.
17. Liebl M, Steinhoff U, Wiekhorst F, Haueisen J, Trahms L. Quantitative imaging of magnetic nanoparticles by magnetorelaxometry with multiple excitation coils. Phys Med Biol. 2014; 59:6607–6620. [PubMed: 25321617]
18. Ludwig F, Heim E, Mäuselein S, Eberbeck D, Schilling M. Magnetorelaxometry of magnetic nanoparticles with fluxgate magnetometers for the analysis of biological targets. J Magn Magn Mater. 2005; 293:690–695.
19. Nakamura K, Ueda K, Tomitaka A, Yamada T, Takemura Y. Self-heating temperature and AC hysteresis of magnetic iron oxide nanoparticles and their dependence on secondary particle size. IEEE Trans Magn. 2013; 49:240–243.
20. Oisjoen F, Schneiderman JF, Astalan AP, Kalabukhov A, Johansson C, Winkler D. A new approach for bioassays based on frequency- and time-domain measurements of magnetic nanoparticles. Biosens Bioelectron. 2010; 25:1008–1013. [PubMed: 19822413]
21. Pankhurst QA, Connolly J, Jones K, Dobson J. Applications of magnetic nanoparticles in biomedicine. J Phys D-Appl Phys. 2003; 36:R167–R181.
22. Pankhurst QA, Thanh NTK, Jones SK, Dobson J. Progress in applications of magnetic nanoparticles in biomedicine. J Phys D-Appl Phys. 2009; 42:224001.
23. Rahmer J, Halkola A, Gleich B, Schmale I, Borgert J. First experimental evidence of the feasibility of multi-color magnetic particle imaging. Phys Med Biol. 2015; 60:1775–1791. [PubMed: 25658130]
24. Richter H, Kettering M, Wiekhorst F, Steinhoff U, Hilger I, Trahms L. Magnetorelaxometry for localization and quantification of magnetic nanoparticles for thermal ablation studies. Phys Med Biol. 2010; 55:623–633. [PubMed: 20071755]
25. Romanus E, Hückel M, Groß C, et al. Magnetic nanoparticle relaxation measurement as a novel tool for *in vivo* diagnostics. J Magn Magn Mater. 2002; 252:387–389.
26. Sarangi S, Tan IC, Brazdeikis A. Brownian relaxation of interacting magnetic nanoparticles in a colloid subjected to a pulsatile magnetic field. J Nanosci Nanotechnol. 2011; 11:4136–4141. [PubMed: 21780417]
27. Sattel TF, Knopp T, Biederer S, et al. Single-sided device for magnetic particle imaging. J Phys D-Appl Phys. 2009; 42:22001.
28. Steinhoff, U.; Liebl, M.; Bauer, M.; Wiekhorst, F.; Trahms, L.; Baumgarten, D. Spatially resolved measurement of magnetic nanoparticles using inhomogeneous excitation fields in the linear susceptibility range ($<$ 1 mT). In: Buzug, TM.; Borgert, J., editors. Magnetic particle imaging. Berlin Heidelberg: Springer; 2012. p. 295-300.
29. Weizenecker J, Gleich B, Rahmer J, Dahnke H, Borgert J. Three-dimensional real-time *in vivo* magnetic particle imaging. Phys Med Biol. 2009; 54:L1–L10. [PubMed: 19204385]
30. Yang TQ, Abe M, Horiguchi K, Enpuku K. Detection of magnetic nanoparticles with ac susceptibility measurement. Phys C-Supercond Appl. 2004; 412:1496–1500.

31. Yoshida T, Ogawa K, Enpuku K, Usuki N, Kanzaki H. AC susceptibility of magnetic fluid in nonlinear brownian relaxation region: experiment and comparison with numerical simulation. Jpn J Appl Phys. 2010; 49:53001.

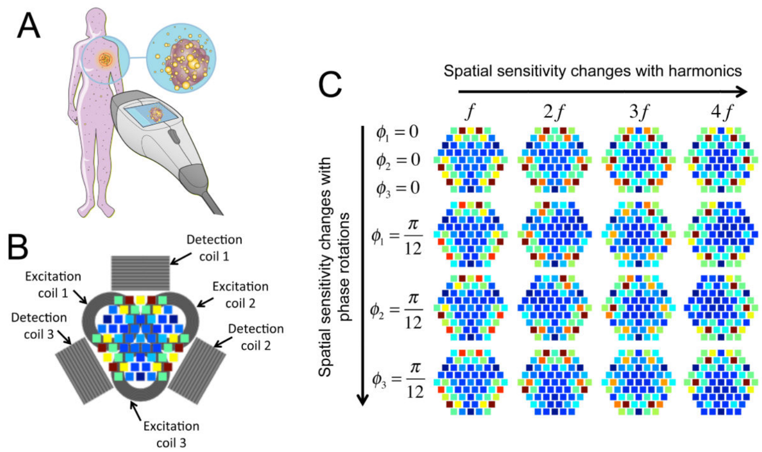

Figure 1.

Conceptual illustrations of a clinical SMI system and the phase encoding scheme that enables high-density imaging with an array of coils. (A) Vision of an SMI system as a low-cost, portable medical diagnostic imager that operates in conjunction with an mNP contrast agent. (B) Excitation and detection coils and the average sensitivity map across the three detection coils for simulated mNP samples. (C) Changes in the spatial sensitivity maps for different harmonics (across) and different phase rotations on the excitation coils (down) can generate a rich data set for tomographic imaging.

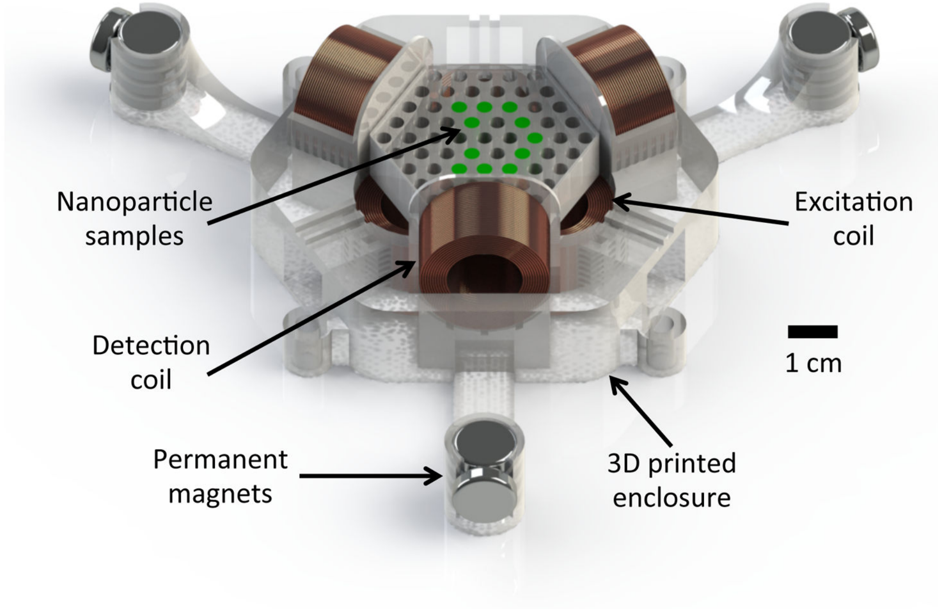

Figure 2.
Rendering of experimental SMI device with labeled detection coils, excitation coils, permanent magnets, 3D printed enclosure, and mNP samples in wells of the imaging grid.

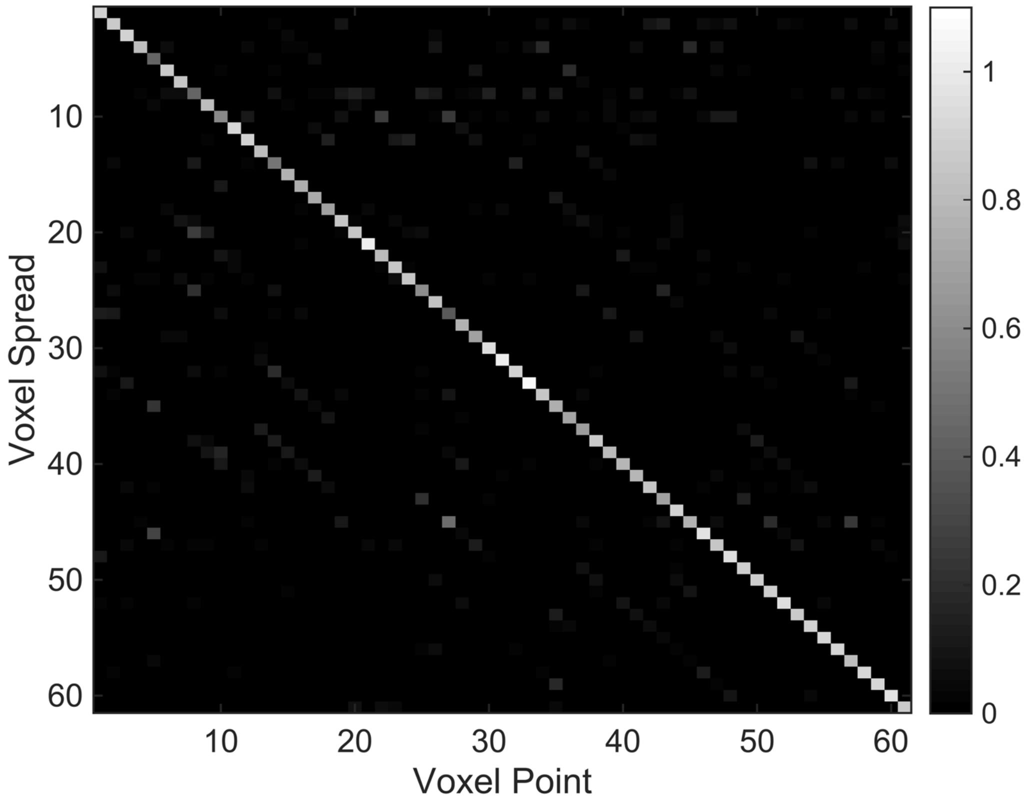

Figure 3.

Point spread functions obtained by multiplying one calibration data set against the inverse of another. The resulting matrix shown has goodness-of-fit $R^2 = 0.92$ with an identity matrix. This illustrates the consistency between placing the samples in each of the 61-voxel locations and then re-positioning them several hours later.

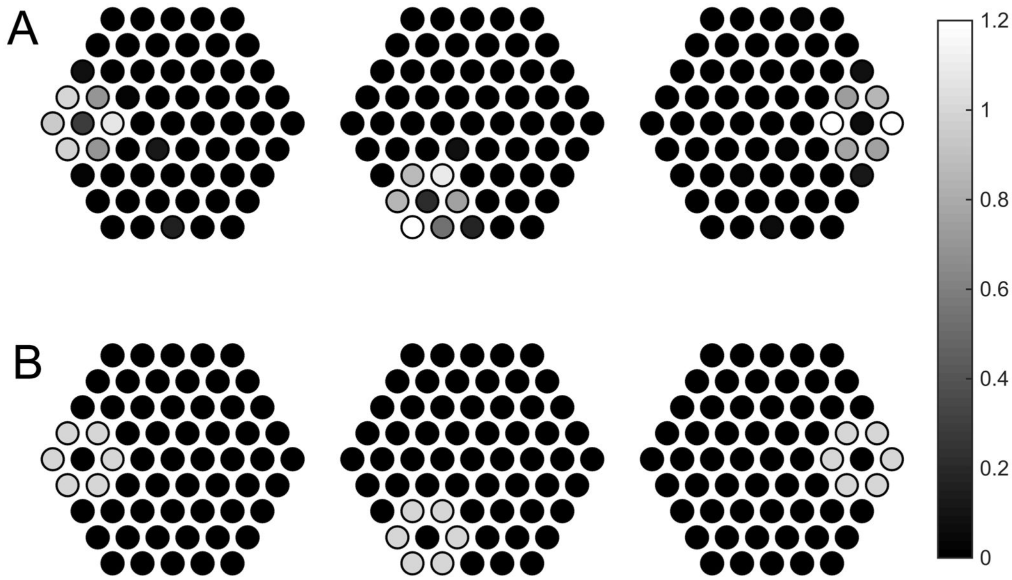

Figure 4.

Image reconstructions of an mNP-filled hexagon positioned around the imaging grid. (A) Imaging results for the mNP-filled hexagon at three positions. (B) Ground truth images for comparison with the imaging results. The goodness-of-fit results between the images in (A) and (B) are R^2 = 0.94, 0.90, 0.92, respectively.

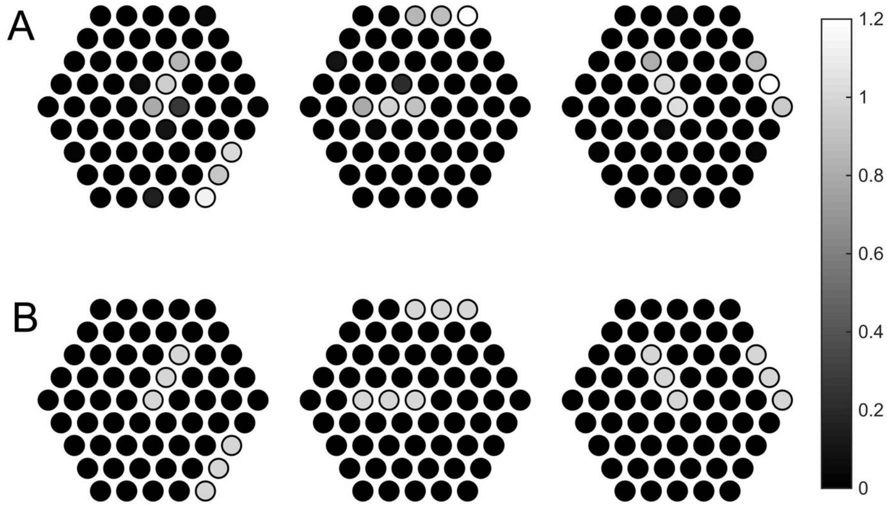

Figure 5.

Tomographic image reconstructions for an mNP-filled two-bar pattern positioned around the imaging grid. (A) Imaging results for the mNP-filled two-bar pattern. (B) Ground truth images for comparison with the imaging results. The goodness-of-fit results between the images in (A) and (B) are R^2 = 0.96, 0.96, 0.97, respectively.

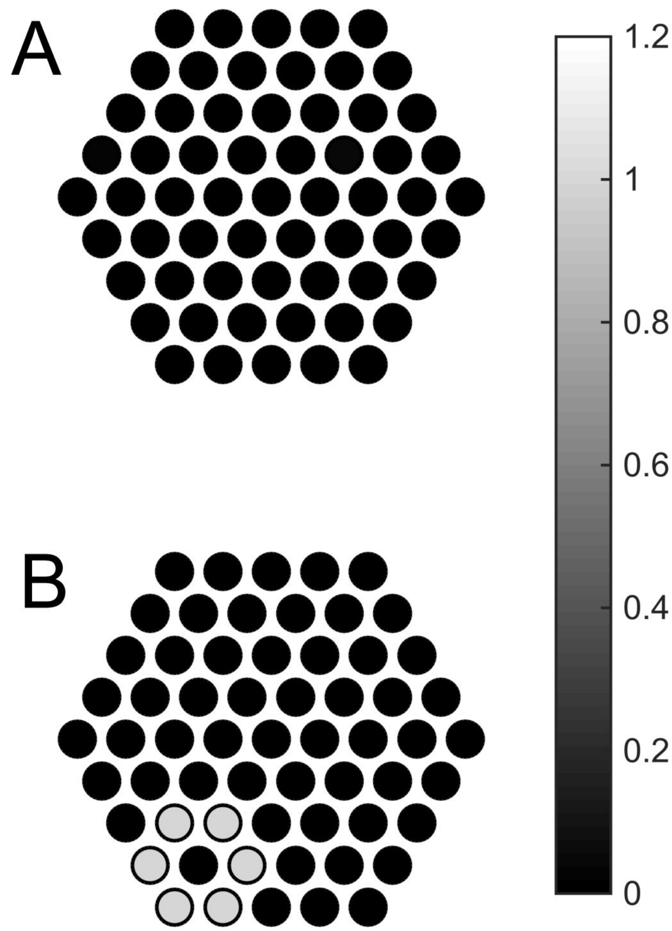

Figure 6.

Image reconstructions for a saline-filled hexagon positioned around the imaging grid. (A) Tomographic image of the saline-filled hexagon. (B) Ground truth image for comparison with the imaging result. The goodness-of-fit between images (A) and (B) is R^2 = 0.01.

Author Manuscript

Author Manuscript

Author Manuscript

Table 1

Phase encoding scheme for the three excitation coils.

Excitation coil	Phase rotation			
	1	**2**	**3**	**4**
1	0, π/2	0, π/2	0, π/2	0, 0
2	0, π/2	0, 0	2π/3, π/2	2π/3, π/2
3	0, π/2	2π/3, π/2	2π/3, 0	0, π/2

Each coil had frequencies of 327 and 350 Hz, which were modulated at each phase rotation.

Table 2

Excitation frequencies and detected harmonic and intermodulation frequencies.

Excitation frequencies (Hz)	Detected harmonic frequencies (Hz)		Detected intermodulation frequencies (Hz)	
	2nd	3rd	2nd	3rd
327, 350	654, 700	981, 1050	677	1004, 1027, 304, 373